Journal of Aerosol Science 42 (2011) 100–113

Contents lists available at ScienceDirect

Journal of Aerosol Science

journal homepage: www.elsevier.com/locate/jaerosci

Simulation of sprayed particle deposition in a human nasal cavity including a nasal spray device

K. Inthavong [a], Qinjiang Ge [a], Camby M.K. Se [a], W. Yang [b], J.Y. Tu [a,*]

[a] School of Aerospace, Mechanical and Manufacturing Engineering, RMIT University, PO Box 71, Plenty Road, Bundoora, Victoria 3083, Australia
[b] Division of Minerals, Commonwealth Scientific and Industrial Research Organization, Blackburn Road, Clayton, Victoria, Australia

ARTICLE INFO

Article history:
Received 27 July 2010
Received in revised form
17 November 2010
Accepted 30 November 2010
Available online 7 December 2010

Keywords:
Nasal cavity
Spray
Deposition
CFD
Modelling
Simulation

ABSTRACT

Effective nasal drug delivery is highly dependent on the delivery of drug from the nasal spray device. Atomisation of liquid spray occurs through the internal atomizer that can produce many forms of spray patterns and two of these, hollow-cone and full-cone sprays, are evaluated in this study to determine which spray pattern produced greater deposition in the middle regions of the nasal cavity. Past studies of spray particle deposition have ignored the device within the nasal cavity. Using computational fluid dynamics (CFD), two computational models of human nasal cavity model were reconstructed from CT-scans, where the difference between the two models was the presence of the nasal spray device accounting for the airway blockage at one of the nostrils. Experimental measurements from Particle Droplet Image Analyser (PDIA) were taken in order to gain confidence in determining the initial particle conditions for the computational models. An airflow field is induced through a negative pressure flow condition applied at the pharynx instead of constant flow rates at the left and the right nasal cavities. Subsequent airflow patterns and its effects on particle deposition, with and without a spray device, are compared. Contours and streamlines of the flow field revealed that the presence of a spray device in the nasal vestibule produced higher levels of disturbed flow, which helped the dispersion of the sprayed particles. Particle deposition was found to be high in the anterior regions of the nasal cavity caused by its inertia. Evaluation of the two spray types found that hollow spray cones produced more deposition in the middle regions of the nasal cavity. This paper also demonstrates the CFD methodology used, which can help in better understanding the design of future atomizers for nasal spray use.

1. Introduction

Nasal drug delivery has long been used for local treatment of the common cold and allergic rhinitis. The nasal route also provides a great opportunity when considering new drug formulations, such as nicotine to assist in smoking cessation, calcium for osteoporosis, or insulin for diabetes. Therefore studies into local droplet deposition are of great significance in the delivery of drugs via the nasal airway. Various studies adopting human subjects or nasal cavity replicas have found relationships for droplet deposition efficiencies with nasal spray parameters, such as the spray cone angle and the droplet size distribution (Cheng et al., 2001; Suman, Laube, Lin, Brouet, & Dalby, 2002). However in-vivo and nasal cavity replica methods are limited in providing detailed results due to the intrusive, time consuming, and expensive nature associated with experimental methods.

* Corresponding author. Tel.: +61399256191; fax: +61399256108.
E-mail address: jiyuan.tu@rmit.edu.au (J.Y. Tu).

0021-8502/$ - see front matter Crown Copyright © 2010 Published by Elsevier Ltd. All rights reserved.
doi:10.1016/j.jaerosci.2010.11.008

Recent developments in medical imaging, e.g. magnetic resonance imaging (MRI) and computed tomography (CT) scanning, coupled with computational science, have opened new possibilities for physically realistic numerical simulations of nasal airflow. Keyhani, Scherer, and Mozell (1995) examined airflow through one side of the human nose in a three-dimensional model that was truncated anterior to the nasopharynx. Subramaniam, Richardson, Morgan, Kimbell, and Guilmette (1998) simulated the airflow structures of the rest and light breathing conditions (15 and 26 L/min) using a laminar flow. Other airflow studies include the work by Zamankhan et al. (2006) and Wang, Denney, Morrison, and Vodyanoy (2005), which briefly discussed airflows through one nasal cavity. Numerical studies provide an alternate method that helps to complement the existing experimental data through a wider range of studies (e.g. repeatability and accuracy of a nasal spray injection released from the same location) that is based on advancements in computational models employing computational fluid dynamics (CFD) techniques.

In recent studies by the authors (Inthavong et al., 2006; Inthavong, Tian, Tu, Yang, & Xue, 2008) sprayed droplet deposition in the nasal cavity was performed based on the characteristics of the atomised drug particles released from a nasal spray. It was found that for a flow rate of 20 L/min 10–20 μm particles are sensitive to initial injection velocity, insertion angle, and spray cone angle as its size is increased. Larger particles exhibiting high Stokes numbers caused it to be insensitive to these spray parameters. In the previous studies the nasal spray device within the nasal cavity was absent from the computational model, while the experimental data did not provide a range of particle sizes.

In this study, which is a step towards establishing more realistic drug delivery simulations, two computational models of human nasal cavity model were reconstructed from CT-scans, where the difference between the two models was the presence of a nasal spray device accounting for the airway blockage at one of the nostrils. Past studies of spray particle deposition have ignored the device within the nasal cavity. An airflow field is also induced from a negative pressure flow condition applied at the outlet boundary (pharynx) instead of equal flow rates between the left and the right nasal cavities. Subsequent airflow patterns and its effects on particle deposition, with and without a spray device, are firstly compared for two nasal spray nozzles (hollow spray cone and full spray cone). Following the flow field analysis, the atomisation of the liquid from a nasal spray device is visually presented to elucidate the external spray characteristics. This is aimed at obtaining a better understanding of the particles, leading to improved initial particle boundary conditions. Additional analysis using a particle droplet image analyser (PDIA) was performed in order to get Sauter mean particle diameters at the near spray nozzle region. This data is important as it provides confidence for setting up the initial particle conditions of the computational model.

2. Methods

2.1. Computational model

An existing computational model of the nasal cavity is used, and for brevity the details of its model construction and verification can be found in Inthavong, Wen, Tian, and Tu (2008) and Inthavong, Wen, Tu, and Tian (2009). In earlier studies by the authors (Inthavong, 2006) among others in the literature (Kleinstreuer & Zhang, 2003; Li, Kleinstreuer, & Zhang, 2007; Straatsma, Van Houwelingen, Steenbergen, & De Jong, 1999), the computational model of the nasal cavity was limited by the available computing power. In this study with increased computing power (HPxw6600 Workstation 16GB Ram, 16 Processors), a nasal cavity with 3.5 million cells (193 Mb in computational memory size) was developed using unstructured tetrahedral cells with mesh refinements at the near wall regions and high curvature geometric features. The finer mesh especially near the wall boundaries allows better modelling of the sharp gradients found in the boundary layer. In addition the maximum y^+ value in any cell of the model is needed to be in the order of 1 (y^+_{max}=0.78) to resolve the near wall region for the low Reynolds number k–ω turbulence model. Grid independence was achieved for a mesh size of 1 million cells (Inthavong, 2006); however it was found that a small percentage of adjacent wall cells had a y^+ value greater than 1, which was addressed in the final model. Based on this nasal cavity model, a second model was created to include the presence of a nasal spray device inside the left nostril. The spray device has a head diameter of 7 mm inserted at an angle from the vertical of 10°. The computational model with a nose spray is depicted in Fig. 1, which consists of 3 regions namely *anterior*, *middle*, and *posterior* regions.

2.2. Fluid flow modelling

Airflow through the nasal cavity was treated as a steady incompressible, isothermal fluid. The two computational models were simulated under a laminar flow for flow rates up to 15 L/min, while above this value the low-Reynolds number k–ω turbulent model was used. For the sprayed particle comparisons a flow rate of 20 L/min was used. Details of the model such as the turbulent viscosity, and the production and dissipation terms can be found in Wilcox (1993) and the Ansys-Fluent documentation (Ansys, 2007). These equations are discretised using the finite volume CFD code, Fluent 6.3.26. The QUICK scheme is used to approximate the momentum equation, whilst the pressure–velocity coupling is handled through the SIMPLE method.

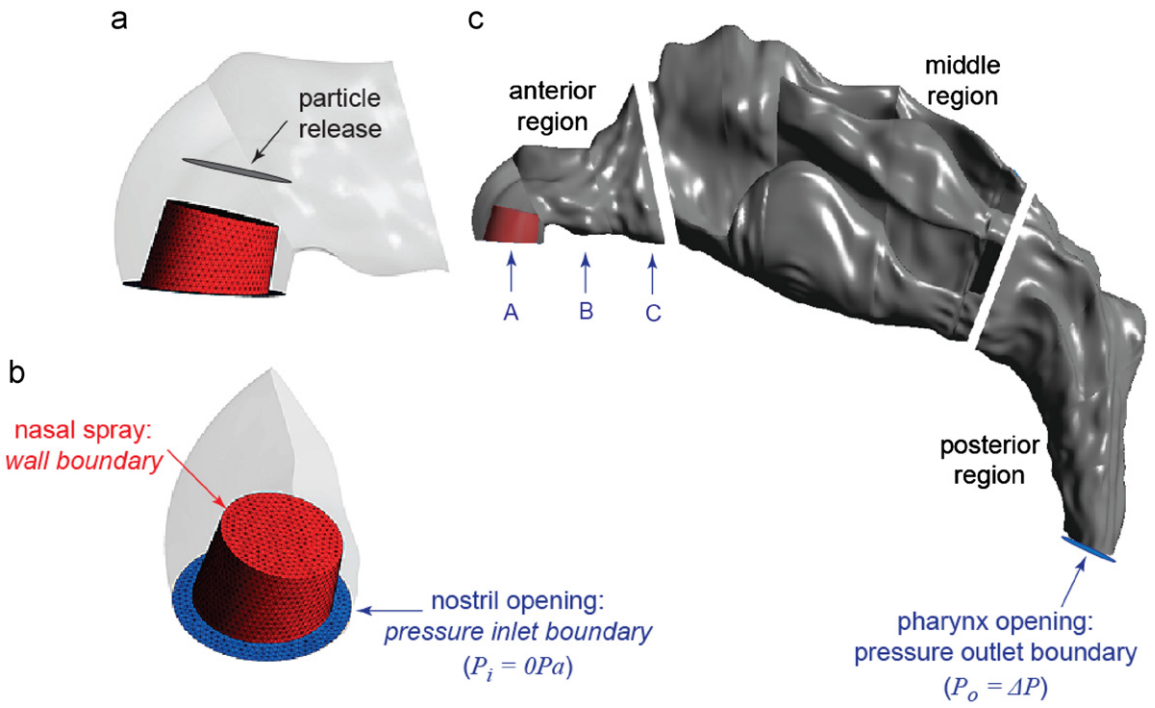

Fig. 1. Computational model inclusive of the nasal spray device, highlighted in red. (a) Particle release region at a distance away from the nasal spray. (b) Cut away of the nostril vestibule where the nasal spray device is inserted. The nasal spray is defined as a wall boundary condition. The blue annulus region represents the surface inlet opening space, left over from the spray device partially blocking the opening. (c) Computational model subdivided into three regions (anterior, middle, and posterior). Labels A, B, C represent three coronal slices in the left nasal chamber created for visualisation of airflow patterns that are located 0.6, 1.6, and 2.5 cm from the nostril tip. (For interpretation of the references to colour in this figure legend, the reader is referred to the web version of this article.)

2.3. Particle phase Modelling

Particles are individually tracked under the Lagrangian approach by integrating the force balance equations on the particle as follows:

$$\frac{du_p}{dt} = F_D(u_g - u_p) + \frac{g(\rho_p - \rho_g)}{\rho_p} + F_s \tag{1}$$

where

$$F_D = \frac{18\mu_g}{\rho_p d_p^2}\frac{C_D \mathrm{Re}_p}{24} \tag{2}$$

$$\mathrm{Re}_p = \frac{\rho_p d_p |u_p - u_g|}{\mu_g} \tag{3}$$

$$C_D = a_1 + \frac{a_2}{\mathrm{Re}_p} + \frac{a_3}{\mathrm{Re}_p^2} \tag{4}$$

where the a's are empirical constants for smooth spherical particles over several ranges of particle Reynolds number (Morsi & Alexander, 1972). The second term in Eq. (1) is the gravity term, while the third term, F_s, represents other possible forces such as virtual mass force, Basset force, pressure gradient force, lift force, thermophoretic force and Brownian force, which are not applicable for micron particles with $\rho_p \gg \rho_g$.

The treatment of one-way turbulent particle dispersions can be performed through a stochastic methodology. The simplest approach and the one available in Ansys-Fluent is the eddy-interaction model (EIM), which is also called the discrete or discontinuous random walk model (DRW). The DRW model is widely used in turbulent particle flows for its conceptual simplicity and uncomplicated reconstruction of the local eddies whose scales are deduced from the local mean flow quantities. The fluid velocity in the particle motion equation (Eq. (1)) becomes $u_g = \overline{u} + u'$. The flow field is then assumed to consist of random discrete eddies, each of which is defined by a lifetime, length, and velocity scale. From the model of Gosman and Ioannides (1981) the eddy scales for homogeneous isotropic stationary turbulence are determined from the fluid

turbulence model as

$$L_e = (C_\mu)^{3/4}\frac{k^{3/2}}{\varepsilon}, \quad \tau_e = \frac{L_e}{(2k/3)^{0.5}} = \sqrt{3/2}(C_\mu)^{3/4}\frac{k}{\varepsilon} \quad \text{and} \quad u_e = (2k/3)^{0.5} \tag{5}$$

Graham and James (1996) suggests that these same representative scales should be doubled for non-homogeneous turbulence as the length and time scales are expected to under-estimate particle dispersion. The fluctuating velocity components $u_i^{'}$ that prevail during the lifetime of the turbulent eddy are sampled assuming that they obey a Gaussian probability distribution. The fluctuating velocity is then

$$u_i^{'} = \zeta\sqrt{\overline{u_i'^2}} \tag{6}$$

where ζ is a normally distributed random number. Assuming that the local root mean square (RMS) velocity fluctuation is isotropy, it can be obtained by

$$\sqrt{\overline{u_i^{'2}}} = \sqrt{\frac{2\kappa_g}{3}} \tag{7}$$

The interaction time between the particles and the eddies is the smaller than the eddy lifetime τ_e and the particle eddy crossing time τ_{cross}. The characteristic lifetime of the eddy is defined as

$$\tau_e = -T_L\log(r) \text{ in which } T_L \approx \frac{0.15}{\omega} \tag{8}$$

$$t_{cross} = -\tau\ln\left[1-\left(\frac{L_e}{\tau|u_g-u_p|}\right)\right] \tag{9}$$

$$\tau_p = \frac{\rho_p d_p^2}{18\mu_g} \tag{10}$$

The particle interacts with the fluid eddy over the interaction time. When the eddy lifetime is reached, a new value of the instantaneous velocity is obtained by applying a new value of ζ in Eq. (6). For one-way coupling the fluid velocity is 'frozen' and the eddy lifetime diminishes to an infinitesimal value as it approaches the wall leading to a build up in particle concentration, an effect which increases as particle inertia reduces. This causes the particles to move very slowly and despite increases in the number of integration steps, they may still not touch the near walls. To alleviate this, different values for the numerical timestep ($\Delta t = 10^{-6}$ s for $\tau_p^+ < 3$ and $\Delta t = 10^{-5}$ s for $\tau_p^+ \geq 3$) were chosen based on preliminary testing in a pipe simulation and the results from Matida, Nishino, and Torii (2000) and Longest and Xi (2007), where τ_p^+ is the normalisation of τ_p by the friction velocity u^* and kinematic viscosity υ_g, given as

$$\tau_p^+ = \tau_p\frac{u_\tau^2}{\upsilon_g} = \frac{\rho_g^2 d_p^2 u_\tau^2}{18\mu_g^2}\frac{\rho_p}{\rho_g} \tag{11}$$

When using RANS turbulence models that are based on an isotropic assumption ($u' = v' = w' = (2k/3)^{0.5}$), the deposition of the small particles ($\tau_p^+ < 10$) is over-predicted. The over-prediction is primarily caused by v', which is much smaller in comparison with the other fluctuating components u' and w'. This can be accounted for by correcting the near wall fluctuations (Matida, Finlay, Lange, & Grgic, 2004; Wang & James, 1999), using the following function:

$$k_{new} = [1-\exp(-0.02y^+)]^2 k \quad \text{for } y^+ < 60 \tag{12}$$

Preliminary pipe flow tests were performed at a Re = 2300 ($\text{Re}_\tau = 56$), which is a similar flow regime to nasal cavity airflows. Fig. 2 shows the v'^+ profile of the isotropic decomposition of k (turbulent kinetic energy), which overestimates the fluctuation in the near wall region. It is evident that the isotropic decomposition over-predicts the v'^+. The near wall correction improves this profile and it is expected to improve the particle deposition also.

2.4. Boundary conditions

Inhalation through the nasal cavity is induced through the pressure difference caused by the movement of the diaphragm compressing and decompressing the lung. Therefore the outlet of the nasal cavity (pharynx) was set as a negative pressure equivalent to 20 L/min relative to the atmospheric pressure at the nostril inlets. The wall boundary condition for the particles was set to 'trap' that all particle trajectories ceased once they touch a wall and the effects of accretion and erosion of particles at the walls are not considered. The sprayed particles adopted the properties of spherical water particles, as most drug formulations are diluted with water. Other assumptions include no particle rebounding off the walls/surfaces, no particle breakup or coagulation, and no particle deformation. The number of particles tracked was checked for statistical independence since the turbulent dispersion is a stochastic process. Particle number independence was deemed for 30,000 particles since an increase to 50,000 particles yielded a difference of 0.1% in the inhalation efficiency.

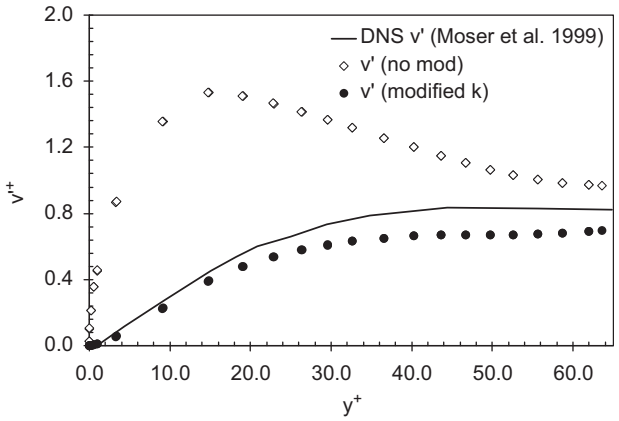

Fig. 2. RMS of normal-to-the-wall velocity fluctuations, v'. The CFD simulation for the k–ω has a Re_τ=56 while the DNS data from Moser, Kim, and Mansour (1999) is shown for Re_τ=180. v' is normalised by the friction velocity (u_τ).

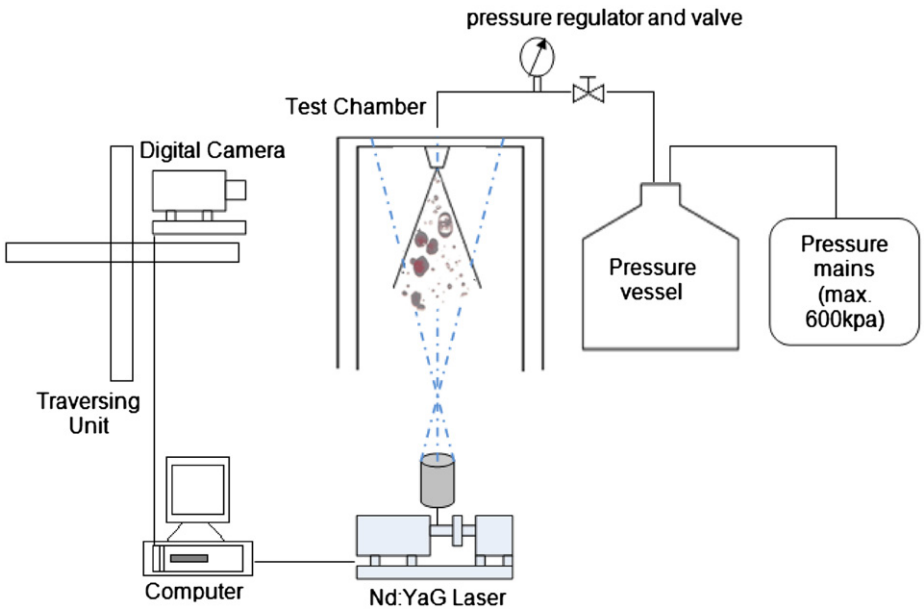

Fig. 3. Schematic of the experimental setup for spray particle measurements.

2.5. Experimental setup

The experimental setup for this study is shown in Fig. 3, which includes a test chamber, a pressurised water supply system, a liquid collection system, and a visualisation system. A particle/droplet image analysis (PDIA) digital image analysis technique by Oxford Lasers® was used, which was capable of determining the properties of individual particles such as its velocity, size, shape, and concentration over a finite region of interest in the flow. For capturing the spray, a double-pulsed Nd:YAG laser was used as the illumination source with a pulse duration of 5 ns. Droplet images were acquired with a non-intensified 12-bit digital camera (PCO Sensicam) and a long distance microscope lens with a magnification of 2.46. This provided a 1280×1024 pixel array to capture a physical region of 3.85 mm $\times$ 3.08 mm. A long distance microscope lens provided a magnification of 2.46 offering a resolution of approximately 3.01 μm/pixel. The camera was mounted on a traversing unit, which allowed precise movements in all three coordinates ($\pm$ 17 μm precision) to reposition the camera in order to capture the spray in full. A constant upstream pressure of 5 Bar was applied and the water was released through a pressure regulator-valve and allowed to reach steady conditions before the images were taken. A single run was limited to approximately 3 min in order to avoid pressure variations associated with a decrease in liquid volume within the pressure tank. The spray nozzle used in the present study was a nasal spray device kindly provided by Saint-Gobain®/Calmar®, Product Number 43110-016.

Diameter measurements in PDIA are based on an area estimate of the shadow image of an individual droplet (straightforward for a perfect sphere). Four commonly used statistical mean diameters are: the number mean diameter, D_{10}; the volume mean diameter, D_{30}; the Sauter (or surface weighted) mean diameter, D_{32}, and the volume weighted mean diameter, D_{43}. The various diameters are defined using the equation:

$$D_{mn} = \left[\frac{\sum d_i^{m-3} V_i}{\sum d_i^{n-3} V_i}\right]^{1/(m-n)} \tag{13}$$

where V_i is the relative volume of droplets with diameter, d_i, and m and n are integer values that describe the mean being used. Thus the Sauter mean diameter, D_{32}, is defined by the equation:

$$D_{32} = \left[\frac{\sum d_i^3}{\sum d_i^2}\right] \tag{14}$$

The Sauter mean diameter was selected to represent the mean diameter of droplets within the flotation cell and is particularly relevant to hydrodynamics and mass transfer, since both drag and reaction rates are proportional to the droplet area.

3. Results

3.1. Computational model validation

Particle deposition efficiencies have been reported in the literature for particles released into the nasal cavity (Cheng et al., 2001; Kelly, Asgharian, Kimbell, & Wong, 2004; Shi, Kleinstreuer, & Zhang, 2007). The deposition of particles as a function of the inertial parameter, ($d_a^2 Q$) is shown in Fig. 4, which displays the characteristic curve associated with inertial deposition. It can be seen among the experimental deposition data in between Cheng et al. (2001) and Kelly et al. (2004) that there is a discrepancy of up to 4X (80% and 20% at IP=10000) which could be due to the subject variability between the nasal cavity models obtained by Kelly et al. (2004) (53-year-old Caucasian male) and the model used in the present study (25-year-old Asian male), while Häußermann, Bailey, Bailey, Etherington, and Youngman (2001) also states that nasal cavity replicate casts with wider airways can cause less deposition due to secondary flow. The DRW model significantly overestimates particle deposition for an inertial parameter (IP) < 10,000. The modification to the model improves the deposition efficiency for better agreement with the reported data for IP < 10,000. In order to gain confidence in our numerical setup, a simple geometry in the form of a 90° bend pipe was also used to investigate the particle tracking model. The 90° bend pipe is useful as the nasal cavity exhibits similar bends at the nostril inlet (anterior) and the nasopharynx (posterior) ends. In this test the data of Pui, Romay-Novas, and Liu (1987) is used (Fig. 5). The results show that the DRW model over-predicts particle deposition for low Stokes number (< 0.1). The DRW with the near wall correction shows that there is a definite improvement to the turbulent tracking model and this provides some confidence to implement the same setup for the nasal cavity model.

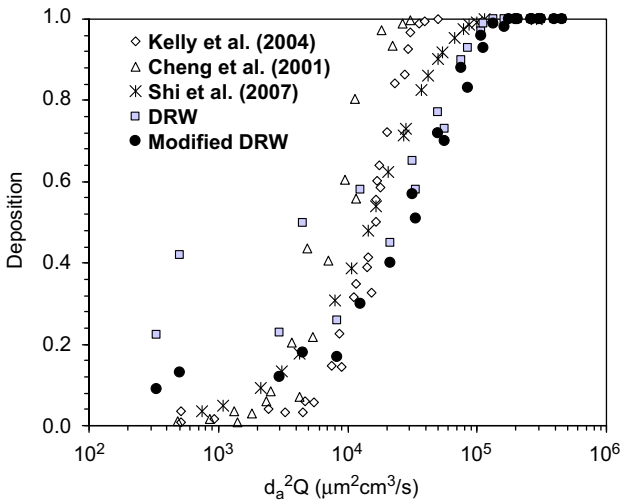

Fig. 4. Inertial deposition efficiency for micron particles in the left cavity side of human nasal cavity compared with the reported data.

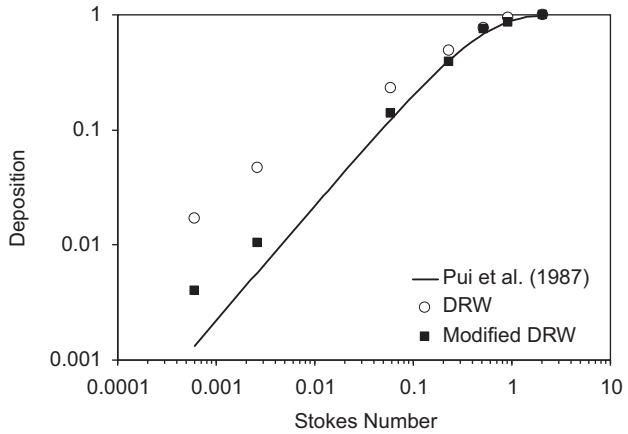

Fig. 5. Particle deposition in a 90° pipe bend for Re=10,000. The depositions by the DRW process and the modified DRW are shown.

Table 1
Mass flow rates induced through a pressure difference between the pharynx (P_i) and the nostril inlets (P=0 Pa).

P_i (Pa)	**Nose model**			**Nose model with spray**		
	Left (L/min)	Right (L/min)	Total (L/min)	Left (L/min)	Right (L/min)	Total (L/min)
5	3.81	4.92	8.73	2.87	5.10	7.97
10	5.81	7.22	13.03	4.44	7.50	11.94
15	7.41	9.01	16.42	5.70	9.37	15.06
20	8.73	10.50	19.22	6.73	10.93	17.67
30	10.97	13.13	24.10	8.55	13.74	22.28
40	12.85	15.37	28.23	10.09	16.05	26.14
60	16.11	19.13	35.24	12.73	19.95	32.68

3.2. Airflow field

Table 1 shows the mass flow rate obtained from the average pressure drop between the nostril and the pharynx ranging from 5 to 60 Pa. At these pressure drops, the corresponding range of Reynolds numbers at the inlets is 981–3951. In both cases the right nasal chamber shows a greater proportion of flow distribution. Further calculations show that the volume of left cavity is smaller by about 13% than the right cavity, which explains the biased distribution between the left and the right airway, which is 44–56% without the nasal spray and 32–68% with the presence of the nasal spray.

Path streamlines that track the fluid motion from the nostril inlet are shown in Fig. 6(a) for a plain nasal cavity model and (b) a nasal cavity including the spray device. For the plain nasal model, the flow streamlines are generally undisturbed as it flows from the nostril inlet and into the nasal valve. The main feature of the flow appears in the nasal valve region where the flow accelerates through the narrowest cross-section of the airway. This region of flow also exhibits some vortical flow proximal to the airway floor as the flow changes direction from a vertical to a horizontal direction due to the 90°-like bend at the nostril. The bulk flow passes mainly through the middle of the cross-section and then partitions into the upper, middle, and lower flow. The presence of the spray device, taking up space in the nasal vestibule, shows an increase in disturbance within the flow. The effective area of the nostril to the open air is reduced and within the narrow air spaces, the flow accelerates through. At the top of the spray, the streamlines separate and swirl through the nasal valve region. Contours of velocity magnitude with streamwise and crossflow velocities superimposed were applied to cross-sectional slices (Fig. 7) taken at the three locations (x=0.6, 1.6, and 2.5 cm from the nose tip) as depicted in Fig. 1. The presence of the spray device causes high velocities in the confined space of the nostril periphery as shown in the path streamlines. At the spray head, the flow field experiences separation and two recirculating vortices are found at the edge of the spray device. At the cross-section B, x=1.6 cm, vortices are present in the lower corners due to the elevation of the geometry. The streamlines show the flow still rising vertically. At cross-section C, x=2.5 cm, the flow patterns are quite different for the two models, which suggests that the influence of the spray nozzle inside the nasal cavity is prevalent up to x=2.5 cm.

3.3. Sprayed particle characteristics

Using a traversing system, a camera with a field of view (FOV) of 3.082 mm × 3.853 mm is moved to ten different positions to capture the entire range of the spray field (Fig. 8a). In the near nozzle region the nasal spray produces a continuous liquid

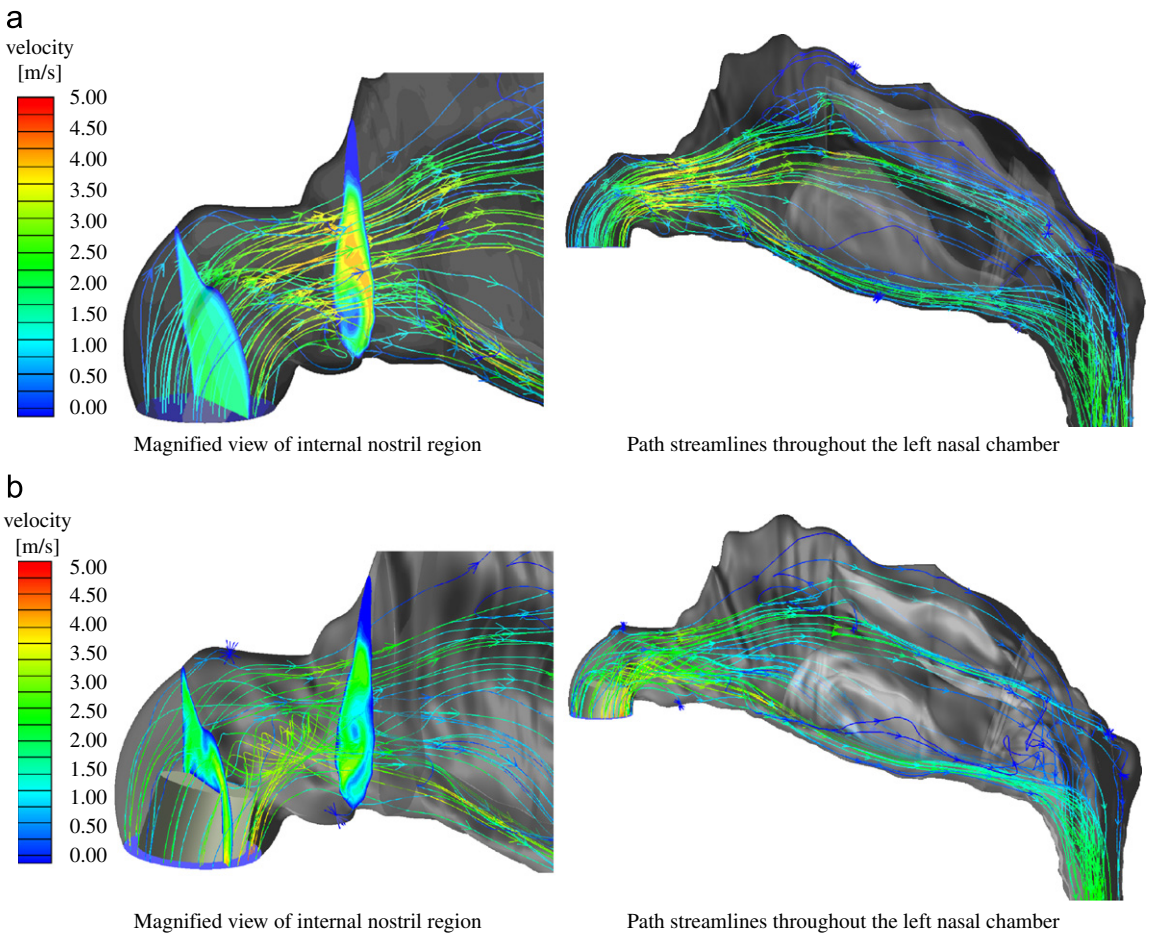

Fig. 6. Path streamlines in the anterior region of the nasal cavity affected by the presence of the nasal spray device. Two cross-sections are shown, one at the spray nozzle and the other at the nasal valve region. (a) Plain nasal cavity model and (b) nasal cavity model with spray device.

stream. The liquid appears to oscillate and roll downstream in waves (Fig. 8b). Further downstream the liquid becomes critically unstable and breaks up into ligaments. The two separate snapshots in time show the destructive change on the liquid sheet as a consequence of the unstable wave on the liquid surface. This initial stage of breakup is called the primary breakup of atomisation. The distance at which clearly formed particles are observed is called the breakup length, which occurs just after the ligament breakup region (between the second and the third row in Fig. 8a). At this location, the particles are dispersed over the spray diameter. This is important for CFD models since the introduction of particles into the computational model needs to be defined at a breakup length rather than as a point source from the nozzle exit (which has traditionally been the case). Additional parameters measured for this particular nasal spray include nozzle diameter ($\sim$0.5 mm), spray cone angle ($\sim 30^{\circ}$), initial particle velocity ($\sim$15 m/s), and breakup length ($\sim$5 mm).

The Sauter mean diameter, D_{32}, was also measured for the bottom two rows of images (Fig. 8a) (the first two rows were not able to be analysed because of the dense liquid region). Eight mean diameters, three along the fourth row and five across the fifth row, are shown in Fig. 9. Larger Sauter mean diameters are located centrally in the bulk spray flow region. In the centre panel at x=0 mm, y=7.705 mm, the largest statistically significant diameter (having at least 0.1% number count) measured was 291–301 μm, while the smallest diameter was 11–21 μm. Further downstream the diameters continue to breakup into smaller particles. This stage of breakup is called the secondary atomisation breakup. In the outer periphery smaller diameters are found. These measurements provide a perspective when setting a range of values for the initial particle boundary conditions in CFD models. In addition a more effective parametrical study can be performed and analysed to provide better guidance in the development stages of nasal sprays for drug delivery. The spray device was included in the model by placing it in the left nasal chamber at an insertion angle of 10° to the vertical axis. The dispersion of the particles is represented by the spray cone angle that was set at an angle of 30°, and the swirl fraction was 0.5, which is only applicable for a hollow spray cone type. Initial tests of particles with nominal mean diameters suggested by the experimental data (e.g. >80 μm) found that all the particles are deposited immediately in the anterior nasal cavity region because of its high inertia. Sprayed particles were introduced into the nasal cavity from a breakup length, L_{bu}, of 4 mm. The spray cone diameter at the breakup length, d_{bul}, was 3 mm, while the initial particle velocity was 15 m/s.

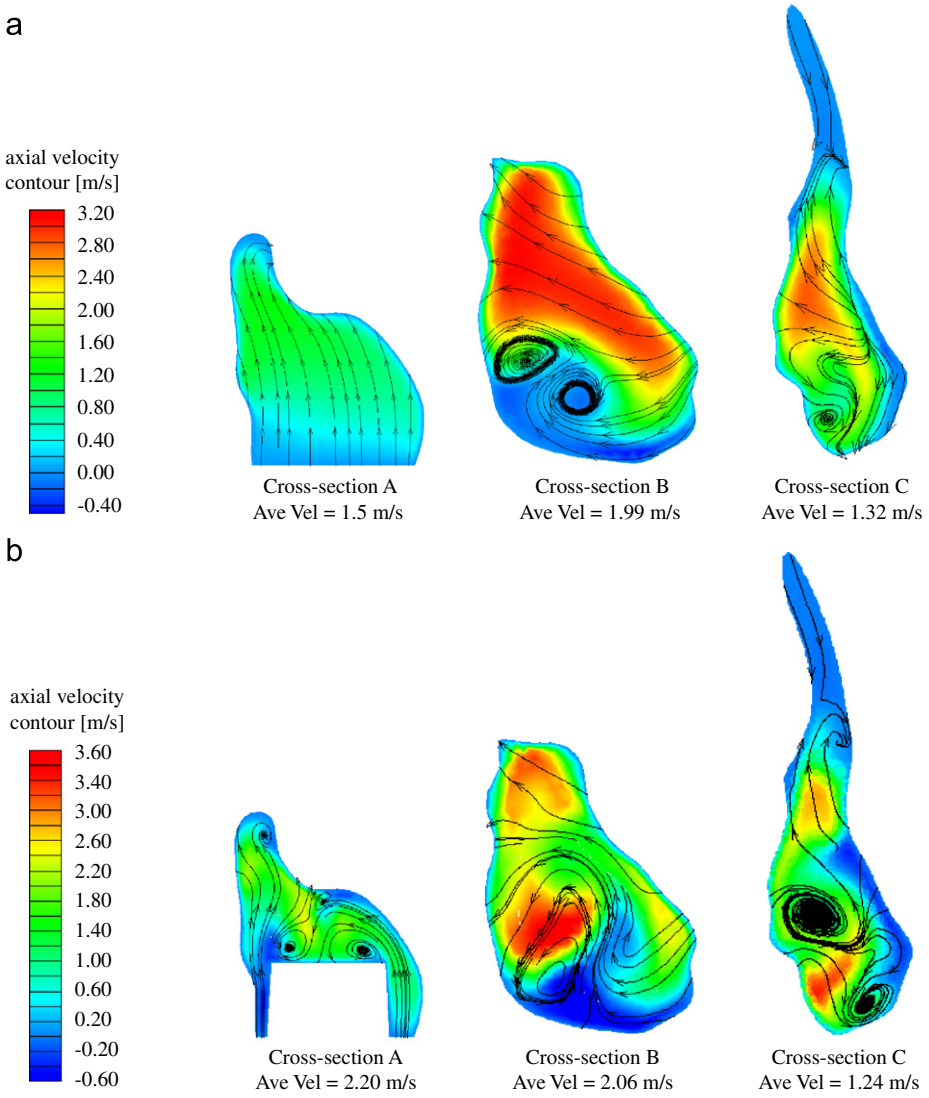

Fig. 7. Crossflow streamlines superimposed onto contours of velocity magnitudes at different coronal cross-sections as defined in Fig. 1. (a) Plain nasal cavity model and (b) nasal cavity model with spray device.

3.4. *Particle deposition*

Sprayed particle deposition in each region (A—anterior region; M—middle region; and P—posterior region) from the two spray types (solid and hollow cones) is shown in Fig. 10. In general there are small differences between the hollow and the solid spray cones. For both the 5 and 15 μm particles hollow spray cones provide greater deposition in the middle nasal region, which may be due to the radial distribution of the particles caused by the swirling component. As the particle size increases so does the particle inertia. For 15 μm particles, the atomised hollow spray achieves 11% deposition in the middle region of the nasal cavity, whereas a solid sprayed cone achieves 100% deposition in the anterior region, and therefore 0% in the middle region. The swirl fraction creates a radial velocity component for hollow spray cones. This helps direct the particles horizontally towards the nasal valve region, leading to increased particle flow through to the middle nasal cavity. For 50 μm particles, maximum deposition occurs in the anterior regions and no particles reach the middle region. For the solid cone spray deposition occurred mainly in the anterior region, while for the hollow cone, more particles were able to deposit in the middle regions. It should also be noted that a large number of 5 μm particles escaped through the pharynx. This will lead to deposition later downstream in the respiratory tract, and may even deposit deep in the lungs, which may have an adverse health response.

The deposition pattern and particle trajectories for the 5 and 15 μm particles are shown in Figs. 11 and 12, respectively. In addition the particle velocity as it impacts the surface walls was recorded and an average value was taken ($V_{pi} = \sum_{i=0}^{N}(v_i/N)$). Note that this average particle impaction velocity, (V_{pi}), is not the same as the deposition velocity, $V^+ = (U_{ave}A/u^*P\Delta x)\log(N_{in}/N_{out})$,

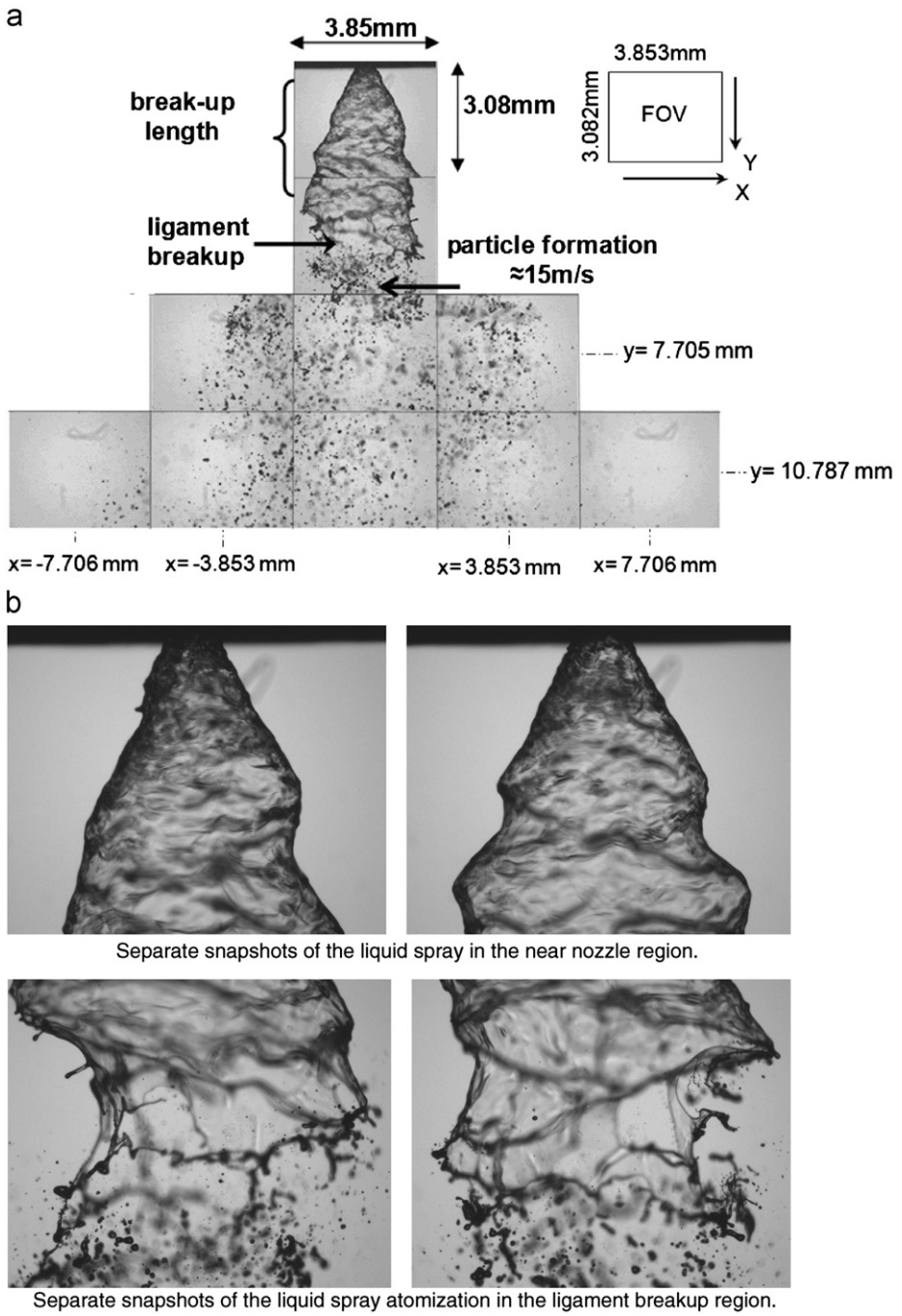

Fig. 8. (a) Microscope scan of the internal spray atomizer nozzle. (b) Instantaneous images with the field of view (FOV) of 3.853 mm × 3.082 mm of the external spray characteristics taken at ten locations and collated together. (c) Two sets of images separated by in time showing the spray particle formation at the near-nozzle region and at the ligament breakup region.

used to characterize the rate of deposition, but rather is a way to determine the influence of the initial particle conditions. The 5 μm deposition patterns for the two spray types are similar and this is evident in the particle trajectories that show similar flow paths. The small differences between the two sprays include a greater number of particles depositing immediately above the spray nozzle for the solid spray cone, which is reflected by the higher V_{pi}. This V_{pi} value suggests that a larger proportion of particles impacts immediately above the nozzle for a solid spray cone. The lower V_{pi} suggests that more particles become entrained in the airflow. The particle trajectories are coloured by particle residence time, which also highlights the looping motion of some particles near the spray nozzle. Some particles that are directed away from the main nasal passage lose enough of its initial velocity and change its direction and gets closer to the nozzle.

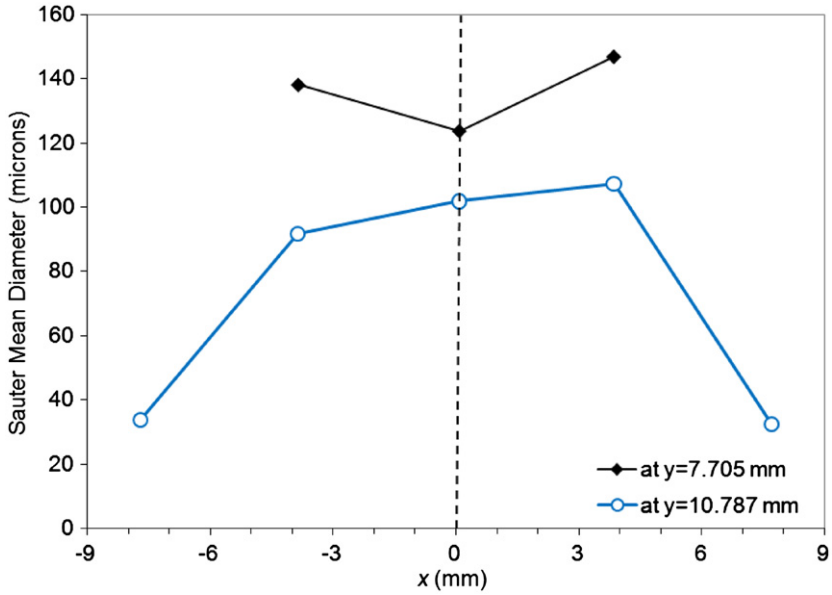

Fig. 9. Sauter mean diameter D_{32} taken for each FOV section or the fourth (y=7.705 mm) and fifth rows (y=10.787 mm) as depicted in Fig. 9b.

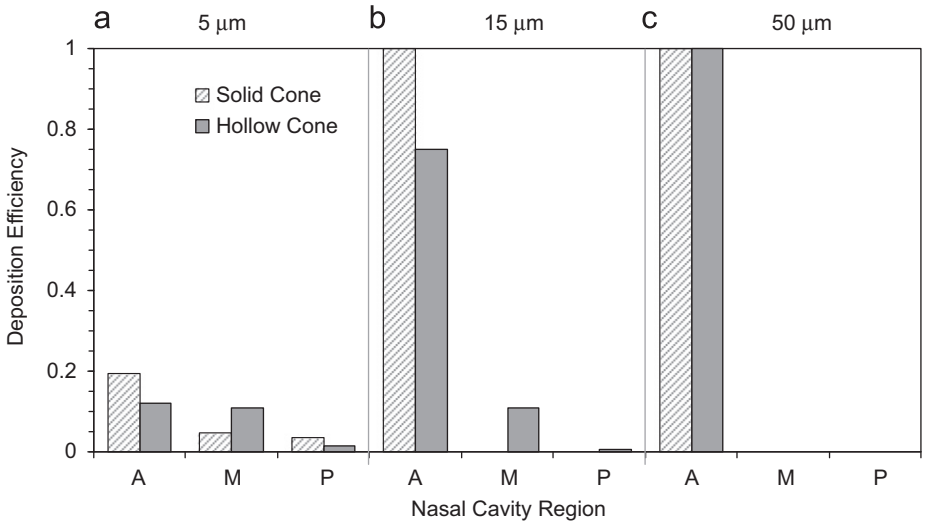

Fig. 10. Sprayed particle deposition from a hollow and a solid spray cone. The x-axis labels, A, M, P represent Anterior, Middle, and Posterior regions, respectively.

15 µm particles have a higher inertial property than a 5 µm particle. The deposition patterns immediately above the nozzle form an outline of the spray type (either solid or hollow spray). While this simulation does not account for particle splattering onto the surface and eventual mucociliary clearance along the nasal walls, it demonstrates the influence of the initial particle conditions (such as the swirl component and the insertion angle) on higher inertial particles. The hollow spray cone allows a small fraction of particles to 'squeeze' through the nasal valve region. It is then inferred that these particles are entrained in the flow before depositing downstream. The V_{pi} for the solid cone shows that on average the initial particle velocity has decreased from 15 to 9.59 m/s over the small distance from particle injection to the upper walls while for hollow sprays this value is 6.64 m/s.

4. Discussion

Sprayed particle deposition between two computational models of nasal cavity is compared, where the difference between the two models was the presence of a nasal spray device inserted into the left nasal chamber. Firstly the airflow distribution and patterns were compared, which found that the presence of the nasal spray device creates additional

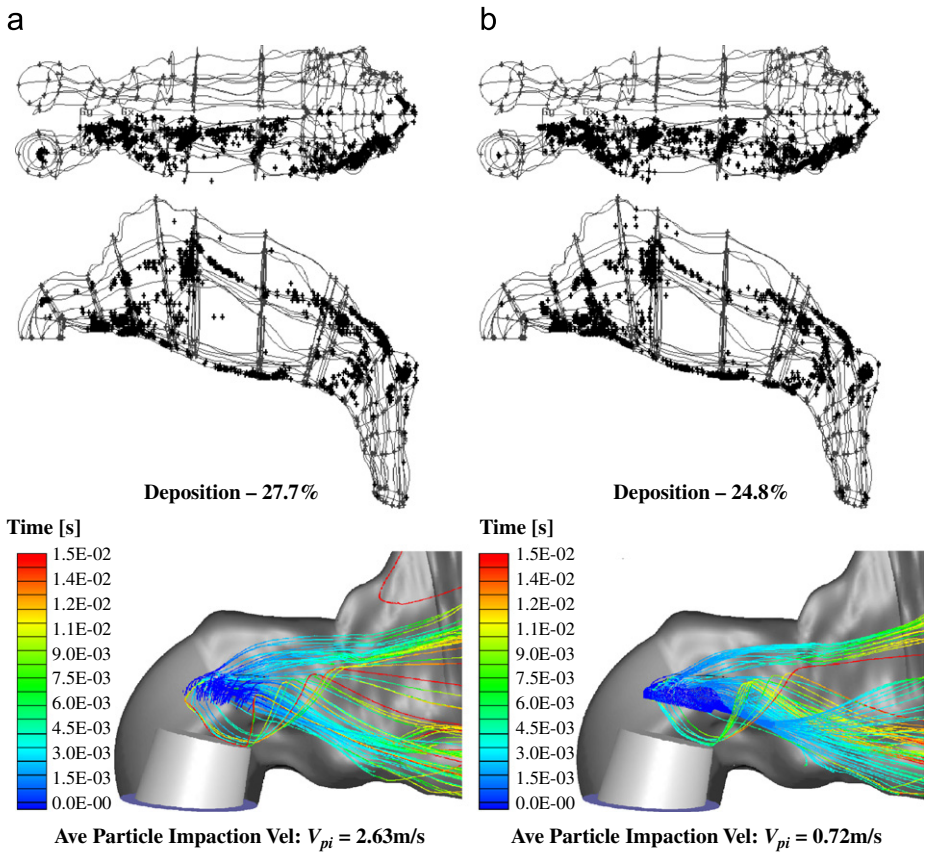

Fig. 11. Deposition pattern of 5 μm in the nasal cavity for solid and hollow spray cones. The particle trajectories are coloured by residence times. (a) Solid cone and (b) hollow cone. (For interpretation of the references to colour in this figure legend, the reader is referred to the web version of this article.)

resistance, obstructing the inhaled air and reducing the flow rate. Furthermore the asymmetrical airflow distribution between the two nasal passages can be attributed to the nasal cycle, which is a result of congestion (swelling) of the erectile tissue (cavernous tissues of the mucosa) in one nasal cavity while at the same time decongestion (shrinking) occurs to the erectile tissue in the other cavity. The airflow through each nasal cavity is then governed by the resistance caused by the cross-sectional area of each airway. Streamlines of secondary flows found that vortices are present in regions of low velocity magnitudes, and in regions of geometry expansion.

Experimental images were then obtained to establish a better understanding of the nasal spray device characteristics. It was deduced that the internal spray atomizer was that of a pressure-swirl type, which is distinguished by the ability to produce greater spray cone angles. The droplet size produced was considerably high having D_{32} in the order of 100 μm in the centre plane of the spray, while at the periphery D_{32} was approximately 30 μm. The particle size produced is a function of liquid pressure and swirl chamber dimensions, where the smaller the swirl chamber is, the finer the resultant droplets can become, but a greater back pressure is needed to force the liquid through the atomizer. The design of the spray atomizer therefore yields significant influence on the particle trajectories.

It is well recognised that one of the functions of the nose is to filter out foreign particulates during inhalation which was mainly thought to be attributed to cilia movement and nasal hairs within the nose. The curvature in the anterior nose along with the constricting nasal valve region is most significant for therapeutic drug delivery as it prohibits larger particles to penetrate into the middle cavity region for deposition onto the highly vascularised mucosal walls. The initial particle conditions from the experimental data showed that the atomised particles are large in size leading to early deposition in the anterior nasal cavity. The particles that are introduced into the airway therefore need to have its inertia stripped away. The swirling fraction that represents the radial component from the swirl atomizer presents the most effective method to reduce the axial velocity. In addition other parameters such as spray cone angle, insertion angle, particle size distribution, initial particle velocity and the location of injection can play a role in the delivery of drug particles. Improvements to the spray atomizer during its design stage may involve atomising the particles at a slower velocity and achieving a much finer particle size distribution. Also instructions for a patient/user may include aligning the spray device more horizontally to the main nasal passage to increase the chances of deposition downstream from the anterior region. This may involve tilting of the head backwards to allow better alignment.

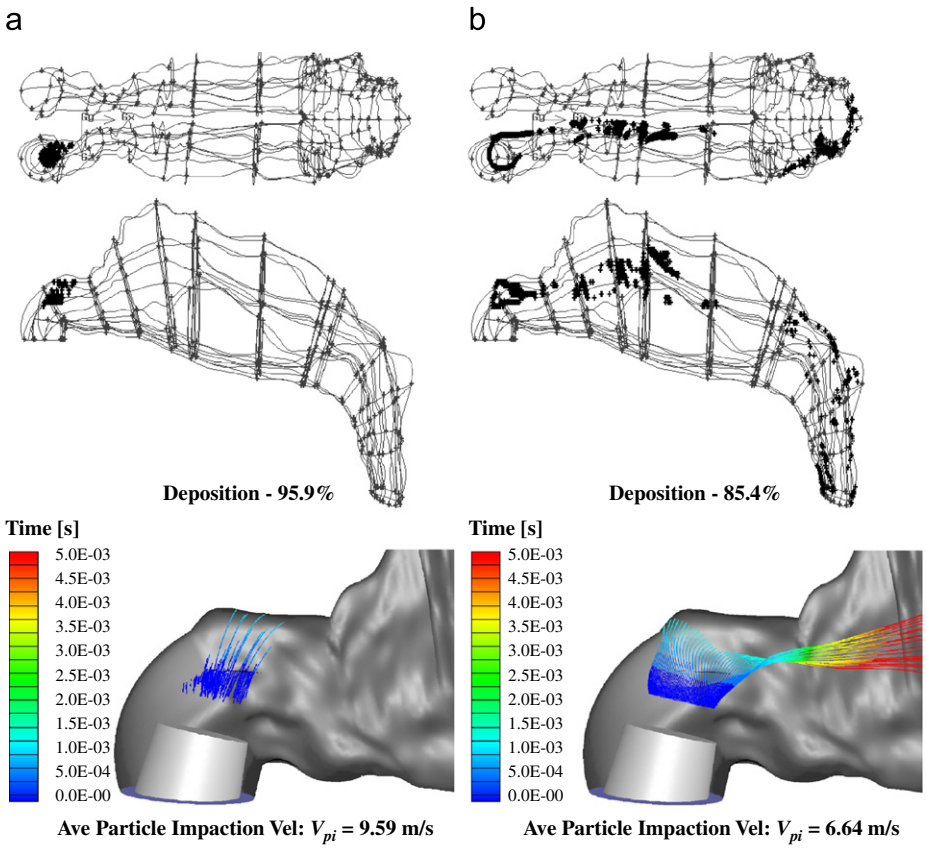

Fig. 12. Deposition of 15 μm in the nasal cavity. The particle trajectories are coloured by residence times. (a) Solid cone and (b) hollow cone. (For interpretation of the references to colour in this figure legend, the reader is referred to the web version of this article.)

Finally, some limitations and improvements of this study need to be noted. In this study one-way coupling is used, which assumes that the flow of particles do not affect the fluid flow. This assumption is valid where the volume fraction of the particles is relatively low ($< 10\%$). This occurs downstream as the particles disperse through the nasal cavity. However near the spray nozzle region (i.e. dense spray region), where the particles are atomising, the volume faction is much higher. The flow field in this region is therefore expected to be under-predicted in the direction that the spray is aligned (10° from the vertical). From the spray images the two-way coupling influence for momentum exchange is limited to approximately 6 mm from the spray nozzle. Turbulence modulation is therefore also not included, which requires an additional loop in the numerical iteration within the current methodology. Other assumptions include no particle breakup or coagulation, no particle deformation, and evaporation.

5. Conclusion

Two computational models of human nasal cavity were produced from CT-scans, where the difference between the two models was the presence of a nasal spray device. This was coupled with the experimental data that was used to provide realistic initial particle boundary conditions. The experimental data was obtained from PDIA measurements, which provided visualisation of the spray development as well as the Sauter mean diameter at different sections of the spray. Important features of the spray characteristics include the spray cone angle, particle size, and the diameter of the spray cone at a breakup length from the nozzle. The measured values provided a basis for setting appropriate initial particle conditions for the computational model. The two nasal cavity models were first simulated to investigate the differences in the airflow field caused by the presence of the nasal spray head. Increased levels of disturbed flow were found where the spray device was placed in the nasal vestibule. The increase in vortices can have two effects: (i) the swirling vortices that have radial and tangential velocities may in fact slow down the linear velocity of the sprayed particles, thereby reducing the particle inertia and (ii) the dispersion of the particles is increased due to the vortices.

Droplet deposition was found to be high in the anterior regions of the nasal cavity caused by the particle inertia, which is a major hindrance for particles to get through the narrow nasal valve region. Evaluation of the two spray cone types found that hollow spray cones produced more deposition in the middle regions of the nasal cavity for 5 and 15 μm particles. For increased efficacy in nasal drug delivery, design issues such as atomisation for finer particle size distribution and slower

initial particle velocity are suggested. In addition instructing the user to align the spray with the main nasal passage may also help. These results demonstrate the use of CFD to provide insight into design issues related to the spray atomizer performance for nasal drug delivery. In addition this work is a step forward towards a more integrated drug delivery simulation that still lacks additional physics such as unsteady inhalation, and further complex physics such as multiphase turbulence and fluid structure interactions.

Acknowledgements

The financial support provided by the Australian Research Council (project ID LP0989452) and RMIT University through an Emerging Researcher Grant is gratefully acknowledged.

References

Ansys, W. C. (2007). *Fluent User Manual*. USA: Ansys Inc.

Cheng, Y. S., Holmes, T. D., Gao, J., Guilmette, R. A., Li, S. Surakitbanharn, Y., et al. (2001). Characterization of nasal spray pumps and deposition pattern in a replica of the human nasal airway. *Journal of Aerosol Medicine*, *14*, 267–280.

Gosman, A. D., & Ioannides, E. (1981). Aspects of computer simulation of liquid-fuelled combustors. In: AIAA 19th Aerospace Sciences Meeting, St Louis, MO.

Graham, D. I., & James, P. W. (1996). Turbulent dispersion of particles using eddy interaction models. *International Journal of Multiphase Flow*, *22*, 157–175.

Häußermann, S., Bailey, A. G., Bailey, M. R., Etherington, G., & Youngman, M. J. (2001). The influence of breathing patterns on particle deposition in a nasal replicate cast. *Journal of Aerosol Science*, *33*, 923–933.

Inthavong, K. (2006). A numerical study into local deposition sites in the nasal cavity for therapeutic and pollutant inhalation. In: Ansys Australasian Users Conference Proceedings 2006.

Inthavong, K., Tian, Z. F., Li, H. F., Tu, J. Y., Yang, W. Xue, C. L., et al. (2006). A numerical study of spray particle deposition in a human nasal cavity. *Aerosol Science Technology*, *40*, 1034–1045.

Inthavong, K., Tian, Z. F., Tu, J. Y., Yang, W., & Xue, C. (2008). Optimising nasal spray parameters for efficient drug delivery using computational fluid dynamics. *Computers in Biology and Medicine*, *38*, 713–726.

Inthavong, K., Wen, J., Tian, Z. F., & Tu, J. Y. (2008). Numerical study of fibre deposition in a human nasal cavity. *Journal of Aerosol Science*, *39*, 253–265.

Inthavong, K., Wen, J., Tu, J. Y., & Tian, Z. F. (2009). From CT scans to CFD modelling—fluid and heat transfer in a realistic human nasal cavity. *Engineering Applications of Computational Fluid Mechanics*, *3*, 321–335.

Kelly, J. T., Asgharian, B., Kimbell, J. S., & Wong, B. A. (2004). Particle deposition in human nasal airway replicas manufactured by different methods. Part 1: Inertial regime particles. *Aerosol Science and Technology*, *38*, 1063–1071.

Keyhani, K., Scherer, P. W., & Mozell, M. M. (1995). Numerical simulation of airflow in the human nasal cavity. *Journal Biomechanical Engineering*, *117*, 429–441.

Kleinstreuer, C., & Zhang, Z. (2003). Targeted drug aerosol deposition analysis for a four-generation lung airway model with hemispherical tumours. *Journal of Biomechanical Engineering*, *125*, 197–206.

Li, Z., Kleinstreuer, C., & Zhang, Z. (2007). Simulation of airflow fields and microparticle deposition in realistic human lung airway models. Part I: Airflow patterns. *European Journal of Mechanics B/Fluids*, *26*, 632–649.

Longest, P. W., & Xi, J. (2007). Effectiveness of direct Lagrangian tracking models for simulating nanoparticle deposition in the upper airways. *Aerosol Science and Technology*, *41*, 380–397.

Matida, E. A., Finlay, W. H., Lange, C. F., & Grgic, B. (2004). Improved numerical simulation for aerosol deposition in an idealized mouth-throat. *Journal of Aerosol Science*, *35*, 1–19.

Matida, E. A., Nishino, K., & Torii, K. (2000). Statistical simulation of particle deposition on the wall from turbulent dispersed pipe flow. *International Journal of Heat and Fluid Flow*, *21*, 389–402.

Morsi, S. A., & Alexander, A. J. (1972). An investigation of particle trajectories in two-phase flow systems. *Journal Fluid Mechanics*, *55*, 193–208.

Moser, R. D., Kim, J., & Mansour, N. N. (1999). Direct numerical simulation of turbulent channel flow up to Re_t=5590. *Physics of fluids*, *11*, 943–945.

Pui, D. Y. H., Romay-Novas, F., & Liu, B. Y. H. (1987). Experimental study of particle deposition in bends of circular cross section. *Aerosol Science and Technology*, *7*, 301–315.

Shi, H. W., Kleinstreuer, C., & Zhang, Z. (2007). Modeling of inertial particle transport and deposition in human nasal cavities with wall roughness. *Journal of Aerosol Science*, *38*, 398–419.

Straatsma, J., Van Houwelingen, G., Steenbergen, A. E., & De Jong, P. (1999). Spray drying of food products:1. Simulation model. *Journal Food Engineering*, *42*, 67–72.

Subramaniam, R. P., Richardson, R. B., Morgan, K. T., Kimbell, J. S., & Guilmette, R. A. (1998). Computational fluid dynamics simulations of inspiratory airflow in the human nose and nasopharynx. *Inhalation Toxicology*, *10*.

Suman, J. D., Laube, B. L., Lin, T. C., Brouet, G., & Dalby, R. (2002). Validity of in vitro tests on aqueous spray pumps as surrogates for nasal deposition. *Pharmaceutical Research*, *19*, 1–6.

Wang, K., Denney, T.S., Morrison, E.E., & Vodyanoy, V.J. (2005). Numerical simulation of air flow in the human nasal cavity. In *Proceedings of the 27th IEEE Annual Conference on Engineernig in Medicine and Biology* (pp. 5607–5610). Shanghai, China.

Wang, Y., & James, P. W. (1999). On the effect of anisotropy on the turbulent dispersion and deposition of small particles. *International Journal of Multiphase Flows*, *25*, 551–558.

Wilcox, D. (1993). *Turbulence Modeling for CFD*. 5354 Palm Drive, La Canada, California: DCW Industries, Inc., 91011.

Zamankhan, P., Ahmadi, G., Wang, Z., Hopke, P. H., Cheng, Y. S. Su, W. C., et al. (2006). Airflow and deposition of nanoparticles in a human nasal cavity. *Aerosol Science and Technology*, *40*, 463–476.